carbon 48 (2010) 949–963

available at www.sciencedirect.com

journal homepage: www.elsevier.com/locate/carbon

A comprehensive scenario for commonly used purification procedures of arc-discharge as-produced single-walled carbon nanotubes

Brigitte Vigolo [a], Claire Hérold [a], Jean-François Marêché [a], Jaafar Ghanbaja [a], Michal Gulas [b], François Le Normand [b,], Robert Almairac [c], Laurent Alvarez [c], Jean-Louis Bantignies [c]*

[a] *Institut Jean Lamour, Department 2, CNRS – Nancy Université – UPV Metz, B.P. 70239, 54506 Vandoeuvre-lès-Nancy, France*
[b] *Institut de Physique et Chimie des Matériaux, Groupe Surfaces et Interfaces (IPCMS/GSI), UMR 7504 (ULP-CNRS), Bat 69, 23 rue du Loess, B.P. 43, 67034 Strasbourg, Cedex 2, France*
[c] *Laboratoire des Colloïdes, Verres et Nanomatériaux (LCVN), UMR 5587 (UM2-CNRS), Université Montpellier 2, Place Eugène Bataillon, 34095 Montpellier, France*

ARTICLE INFO

Article history:
Received 13 August 2009
Accepted 30 October 2009
Available online 5 November 2009

ABSTRACT

The purification of single-walled carbon nanotube (SWCNT) samples was analysed using a multi-technique approach, with structural as well as spectroscopic probes, in order to characterize the samples and to identify important factors for improvement of SWCNT sample quality. The first dry oxidation step (air at 365 °C) is shown to have only a weak selectivity for the removal of the amorphous carbon or weakly organized graphitic species as well as resulting in a partial consumption of the SWCNTs. The functionalization of the SWCNTs is highly specific with formation of carboxyl, hydroxyl and carbonyl groups. On the other hand this oxidation step is highly efficient for the oxidation of the catalytic impurities (Ni, Y) which can be easily removed by subsequent acid treatment. A final high temperature treatment indicates some incomplete restoration of the quality of the SWCNT surface.

1. Introduction

Carbon nanotubes with unique structural and physical properties represent exciting opportunities for fundamental science and new technologies [1]. Development and progress in the synthesis methods of large-scaled production of single-walled carbon nanotubes (SWCNTs) over the past decade have opened many potential applications such as energy storage media, nanocomposites or electronic nanodevices. An undesirable outcome of many growth processes that produce SWCNTs is that the samples contain residual growth catalyst and carbonaceous particles as major impurities. It is a challenging problem to efficiently purify samples without damaging the tubes. More accurately, pristine SWCNTs samples persistently contain several kinds of heterogeneities: (i) other graphitic or carbon phases, like fullerenes, amorphous carbon, graphitic ribbons and particles, . . .; (ii) impurities such as residual metallic catalysts, often protected by more or less graphitized carbon shells and polyhedra; (iii) surface defects at the SWCNT surface or oxygenated grafted functions, (iv) dispersion in diameter, chirality and morphology (aspect ratio) and (v) aggregation into bundles. These heterogeneities represent a major obstacle for both the establishment of universal behaviours and the development of optimized processing methods for CNT purification. The used purification process must lead to an improvement of the sample quality

* *Corresponding author:* Fax: +33 3 88 10 72 48.
E-mail address: Francois.Le-Normand@ipcms.u-strasbg.fr (F.L. Normand).
0008-6223/$ - see front matter
doi:10.1016/j.carbon.2009.10.044

regarding: (i) the increase of the amount of SWCNTs over the total mass of the sample by removing other carbon phases and metallic impurities and (ii) reducing the defect number at the SWCNT surface which is often damaged due to the purification steps [2].

Several methods have been optimized for the bulk synthesis of SWCNTs. Among them, arc discharge is able to produce SWCNTs with fewer structural defects than those obtained by low temperature techniques such as CVD-based techniques. Moreover, the diameter distribution of arc-discharge-produced SWCNTs is rather narrow. Nevertheless a robust and reliable postsynthesis chemical purification is still required for the improvement of the sample purity and quality. The purification procedures usually follow three main steps [3–18]. Sample is first submitted to an oxidation treatment, either wet like H_2O_2 or dry like air thermal treatment, which is usually used to remove carbon impurities and to weaken carbon shells protecting catalytic particles. These latter ones become then accessible to a subsequent solubilisation through an acid treatment. The optimization of the two first steps controls the weight loss of the sample. These chemical treatments also unconveniently lead to the formation of organic functions and of structural defects at the SWCNT sidewalls, in addition to their partial consumption. Thus a final high temperature annealing is necessary to restore the sp^2 SWCNT structure. The SWCNT preparation and purification have important implications on their properties. As an example, the tensile strength of the CNTs synthesized by a CVD method is only one tenth of those grown by arc discharge [19]. It is subsequently of paramount importance to follow, throughout the purification procedure, the sample changes both in impurities (concentration, nature, morphology, ...) and in the SWCNT characteristics (surface properties, crystallinity, defects, surface functions ...).

In this paper, we have investigated a commonly used three-step purification procedure to commercial arc-discharge-produced SWCNTs. Special care is taken to get a complete characterization of the samples after each chemical treatment of the procedure. The approach is based on the use of several complementary techniques sensitive to both the residual impurities concentration and the SWCNT surface quality: transmission electronic microscopy (TEM), X-ray diffraction (XRD), thermogravimetric analyses (TGA), Raman, infra-red, photoemission (XPS) and Near Edge X-ray Adsorption Fine Structure (NEXAFS) spectroscopies. The procedure is reproducible and robust for finding out a comprehensive scenario for this multi-step purification process and for allowing identifying important factors for further optimization.

2. Experimental

2.1. *Sample preparation and purification procedure*

The SWCNT samples used in this work were synthesized by an arc-discharge method and were provided by Carbolex Inc. The purification procedure followed was simplified from Furtado et al. [20]. It consisted in the three steps commonly used for purification of arc-discharge samples: (i) thermal oxidation in dry air. The soot was placed in a silica crucible and oxidation was done at 365 °C for 90 min under air (flux of 100 ml/min) dried over a $CaCl_2$ column. Using water-free air allows achieving selective dry oxidation of amorphous carbon and avoiding the formation of hydrogenated functions, such as alcohol, more stable than ketone or ether groups. This first step (step i) was also expected to weaken carbon coating of the metal particles combining two mechanisms: a simple chemical attack of the carbon shells and a mechanical stress due to possible dilatation of the catalytic core through oxidation. This was especially the case for nickel. The second step (step ii) was an acid treatment in a hydrochloric acid (HCl) solution (6 N) for 24 h under reflux. The pH was thereafter increased to neutralization with a filtration/washing process. Metallic oxides were expected to be solubilised in the acid solution and eliminated from the sample during the filtration. Filtration was done with a 2 μm pore size polycarbonate membrane filter and the deposited solid was washed several times with pure water until pH of 6–7 was attained. The soot was then dried at 50 °C overnight. The third step (step iii) consisted in a high temperature (HT) treatment under vacuum. Temperature was progressively increased from room temperature up to 1100 or 1400 °C, and then stabilized for 1 h. During the raising stage the sample had a tendency to outgas. The temperature was then increased step by step as soon as the pressure is stabilized. Pressure was kept below 1.10^{-4} mbar during the whole annealing process. The average weight losses are 60, 90 and 15 wt.% after steps i, ii and iii, respectively. Samples were characterized after each step of the purification procedure. Raw sample was named PS0. PS1 and PS2 were the samples after the step i and step ii described above, respectively. PS3a and PS3b corresponded to the samples obtained after the thermal treatments at 1100 and 1400 °C, respectively.

2.2. *Sample characterization*

2.2.1. *Infra-red spectroscopy*

Fourier transform infrared (FTIR) experiments were carried out on a Bruker IFS 66V spectrometer equipped with a N2-cooled MCT (Mercury Cadmium Telluride) detector. Transmission IR spectra were recorded in the 400–4000 cm^{-1} range. The spectral resolution was 2 cm^{-1} and 64 scans were co-added for each spectrum.

2.2.2. *Raman spectroscopy*

Raman spectroscopy study has been performed using a T-64000 Jobin–Yvon apparatus and two excitation wavelengths (514.5 and 647.1 nm).

2.2.3. *NEXAFS*

The Near Edge X-ray Absorption Fine Structure (NEXAFS) experiments were carried out at the BEAR beamline of Elettra synchrotron radiation facility (Trieste, Italy). The spectral resolving power ($E/\Delta E$) of incident photons at 400 eV was 800. The X-ray spot area was 0.01 mm^2. Spectra were recorded in the total electron yield mode in an ultrahigh vacuum chamber. The solid powder of nanotubes was pressed on a metal plate thanks to indium. The samples were outgased for 3–4 h before the recordings.

2.2.4. XPS

XPS was performed on an AXIS Ultra DLD XPS apparatus equipped with an Al K_α monochromatic source. Base pressure was 1.10^{-9} mbar. The energies were calibrated to the main C1s peak referred at 284.6 eV. With such reference, the energy shift due to surface polarization was negligible, at the notable exception of the first treatment of oxidation. Spectra are both corrected with a Shirley background and deconvoluted by a Voigt function, accounting for experimental resolution and finite lifetime of the excited core levels. The overall resolution was estimated to 0.75 eV. The relative concentrations (atomic%) were deduced from the surface intensities corrected by the photoionization cross-sections set as 1, 2.93, 5.98 and 22.18 at the C1s, O1s, Y 3d and Ni 2p core levels, respectively [21].

2.2.5. XRD

X-ray data were obtained with a powder diffractometer equipped with a Cu K_α X-ray source, a flat germanium crystal monochromator and a 2-D position sensitive detector INEL CPS-120.

2.2.6. TGA

TGA analyses were performed on a SETARAM TGA92 setup with dried air (N_2:O_2 at 78:22 mol:mol) at a rate of 5 °C/min from room temperature till 900 °C with around 1 mg of initial sample.

2.2.7. TEM

Transmission electron microscopy (TEM) using a Philips CM 20 apparatus at an operating voltage of 200 kV was carried out to follow qualitatively changes of SWCNTs and impurities. For the observations, raw and treated SWCNTs after each step of the purification procedure were dispersed in ethanol in a low-power sonication bath for a few minutes and deposited on a holey grid (300 mesh size). In order to obtain a statistical view of the samples, several zones (about 10) were observed for each sample.

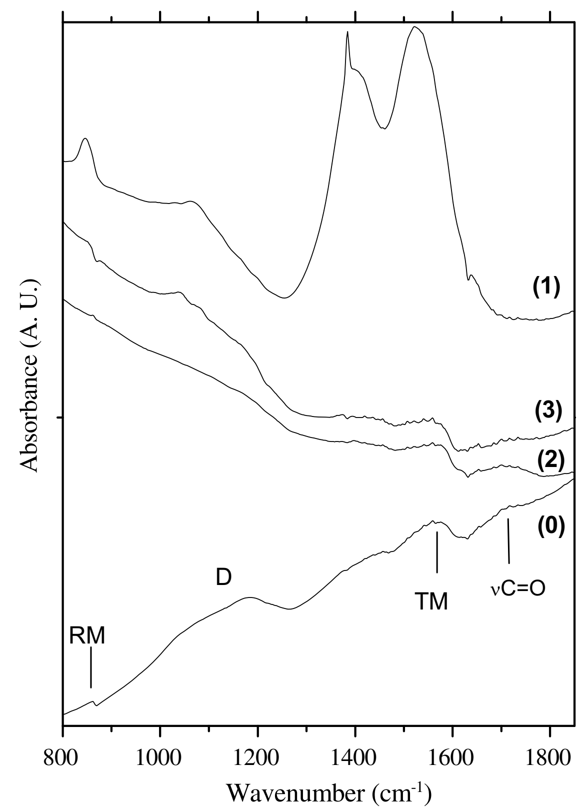

Fig. 1 – Infra-red spectra of the nanotubes: (0) PS0; (1) PS1; (2) PS2 and (3) PS3b samples, respectively.

3. Results and discussion

3.1. *Functional groups introduced at the SWCNT surface through the chemical treatments*

3.1.1. *Infra-red absorption spectroscopy*

The 800–1800 cm^{-1} wave number range of the IR absorption spectra measured on SWCNT samples during the different purification processes are compared in the Figs. 1 and 2. In the pristine sample PS0 (spectrum noted (0)), as expected small features centered around 1590 and 860 cm^{-1} corresponding to the tangential (TM) and radial modes (RM) of the SWCNTs are evidenced, respectively [22]. The wide component centered around 1200 cm^{-1} corresponds to the D-band ascribed to structural defects [23]. Around 1720 cm^{-1}, a peak assigned to the stretching mode of the carbonyl vibrations ν(C=O) is shown. This fingerprint signs the presence of oxygenated species in the pristine sample. No conclusion can be done concerning the presence of carboxylic acid species due to the difficulty to detect the intramolecular hydroxyl stretching vibrations ν(O–H) in the high frequency domain within 3000–4000 cm^{-1}. This range is polluted by the ν(O–H) vibrations corresponding to adsorbed water and the one due to the hygroscopic transparent IR medium. After oxidation (spectrum (1) of sample PS1 in Fig. 1), a dramatic modification of the spectra is exhibited showing the appearance of new large contributions. Two broad bands are shown respectively around 1400 and 1521 cm^{-1} and are attributed to the bending vibration of the Ni–O–H groups [24]. This attribution is confirmed by the presence below 600 cm^{-1} of a broad contribution corresponding to NiO lattice vibrations [25]. From XPS and X-ray diffraction results (Sections 3.1.4 and 3.2.1, respectively), we know that the presence of NiO can be responsible of such behaviour. The signal coming from the carbon atoms is totally hidden by this new phase. This is the reason why no conclusion can be done regarding the precise state of the SWCNT surface for sample PS1 based on IR absorption spectroscopy. These features have been previously observed after dry oxidation [26].

HCl refluxing treatment is expected to be highly reductive toward the sample. However, for sample PS2, a significant enhancement of the ν(C=O) compared to the raw sample can be detected (sample PS2 (2) in Fig. 2a), meaning that the oxygenated surface groups introduced through the first step of the procedure have not completely been removed by the acid treatment. As a result, the number of oxygenated groups in the sample PS2 is higher than in the raw sample (PS0). After vacuum heating the ν(C=O) features disappear (spectrum (3)

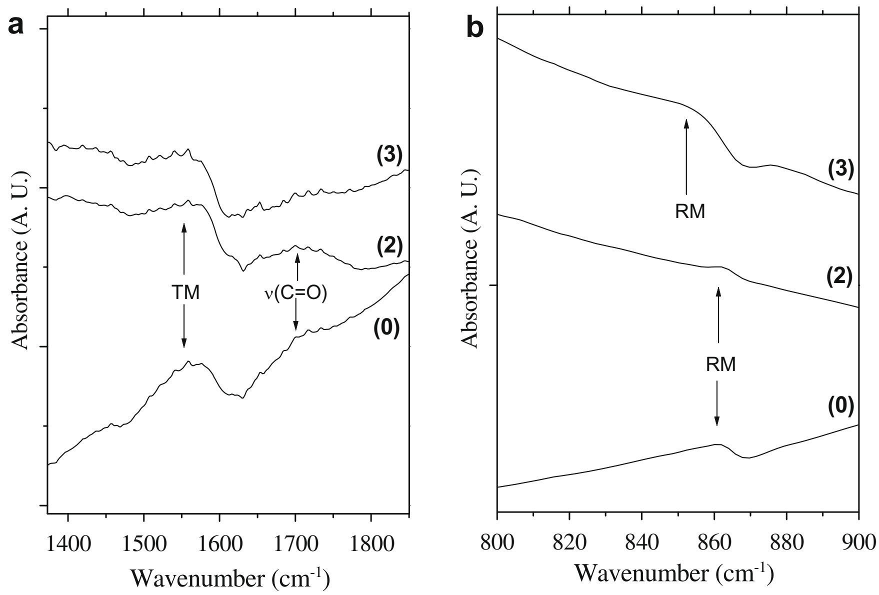

Fig. 2 – IR-active tangential modes: (a) and radial modes (b) of the (0) PS0; (2) PS2 and (3) PS3b samples, respectively.

in Fig. 2), signing the efficiency of the purification concerning the removing of the oxygenated surface defects. The relative proportion of the oxygenated carbonyl species compared to total carbon during the different steps of purification is hazardous due to the absence of reliable normalization band for all spectra. XPS and NEXAFS spectroscopies, as it will be seen further, are very complementary probes, due to the atomic selectivity, to study more quantitatively the oxygenated impurities at the surface of the tubes.

Concerning the carbon vibration features, the broad TM modes around 1590 cm^{-1} (Fig. 2a) are not sensitive to the purification process as expected [22]. In the range of the radial modes (RM) (Fig. 2b), the band is localized around 860 cm^{-1}. After HCl treatment, a decrease of the intensity of the RM modes relative to the TM modes is shown. This result suggests a deep modification of the dynamical dipolar momentum associated to the presence of a higher content of carbonyl defects at the surface of the tubes. After vacuum heating, a broadening of the RM modes concomitant to a small downshift (peak centered around 855 cm^{-1}) is shown. The RM modes are known to be the more sensitive to the structure of the tube [22]. They are also clearly the most sensitive to the purification process. In the range of the wide D-band, around 1150 cm^{-1}, the intensity of the very broad structure decreases as expected after air oxidative and HCl treatment. An increasing of the D-band after vacuum heating is shown compared to the HCl treatment concomitant of the broadening of the TM modes discussed above.

3.1.2. *Raman analysis*

The Raman spectra are displayed on Fig. 3a and b with special emphasis on the Radial Breathing Modes (RBM around 160 cm^{-1}), the D-band (around 1350 cm^{-1} and the tangential modes (G band at 1590 cm^{-1}). The peak evolutions as a function of the purification treatment are quite similar whatever the excitation wavelength. We can first note that after the first step of the procedure the relative intensity of the larger tubes increases with respect to the smaller ones in the RBM region. This could indicate that the small tubes are more sensitive to the oxidation treatment. A stretching of the carbon nanotubes inside the bundle can also be invoked. It should be noticed that the downward shift of the RBM is accompanied by a homogenization of the size distribution of the SWCNTs (Fig. 3b).

Further information might be derived from the behaviours of both the D and the G bands. After the first step of purification the former one gets sharper, undergoes a slight upshift and a decrease of its intensity. This trend, confirmed after the second step, is consistent with the removing of carbonaceous impurities. However, after the high temperature annealing, the D-band downshifts and becomes more intense as if the SWCNTs were damaged by the high temperature treatment. The main peak of the G band also upshifts but only after the second step. This behaviour has been already observed for multi-walled nanotubes but is not yet clearly understood.

3.1.3. *NEXAFS results*

NEXAFS spectroscopy is then used to investigate the nature of the interactions between functional groups and SWCNTs at each step of the functionalization process. Fig. 4 shows the C K-edge spectral region in SWCNTs before and after the different steps of purification. The spectra of pristine sample PS0 is dominated by a sharp C–C 1s $\rightarrow \pi^*$ transition at 286 eV corresponding to hybridized sp^2 carbon. The excitations between 292 and 315 eV are associated with mainly overlapped 1s $\rightarrow \sigma^*$ transitions. The domain between 287 and 291 eV is particularly interesting in our case since it evidences the chemical modification of SWCNTs by functionalization [27].

After oxidation (see right inset in Fig. 4), the spectrum is dominated by a new contribution discussed below. One can notice that in the case of sample PS2 after oxidation and

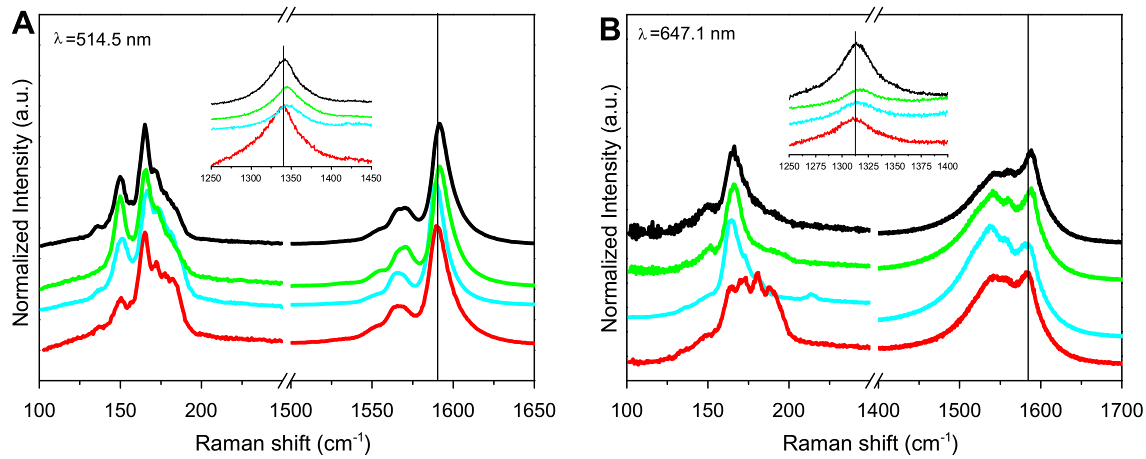

Fig. 3 – Raman spectra of the samples after each step of the purification procedure. (A) λ = 514.5 nm; (B) λ = 647.1 nm. From bottom to top: PS0, PS1, PS2 and PS3a samples, respectively. The D-band range is displayed in inset.

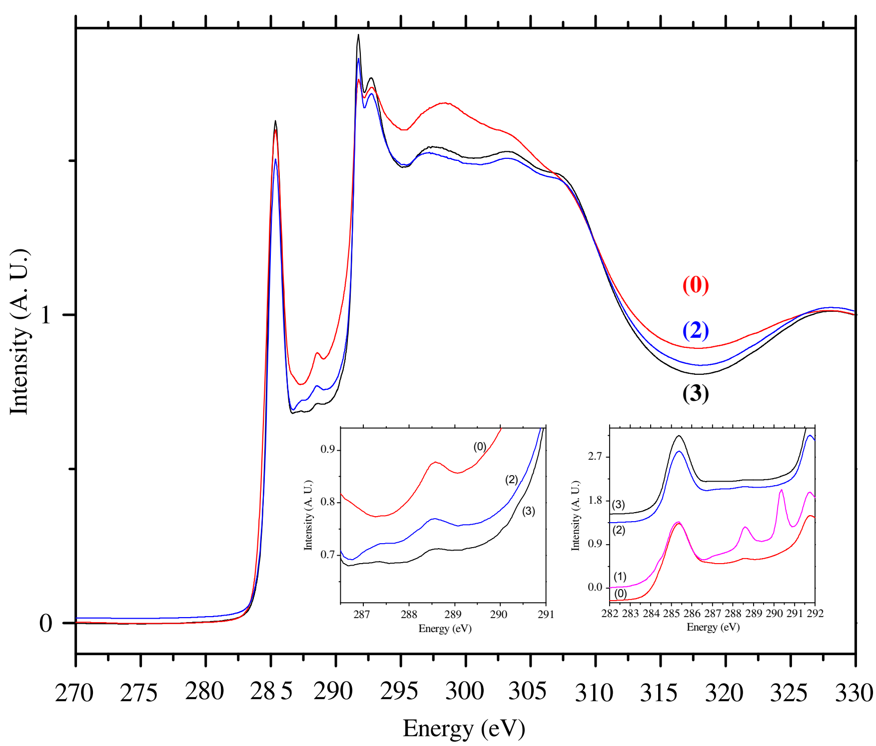

Fig. 4 – C K-edge NEXAFS spectra at different step of the purification process (0) PS0; (2) PS2 and (3) PS3b samples, respectively. Left inset: region of the $\pi \rightarrow \pi^*$ excitations of functionalized groups. Right inset: Superimposition of the spectrum PS1 in the region of the $\pi \rightarrow \pi^*$ excitations.

HCl treatments, two resonances around 287.4 and 288.6 eV are exhibited (see inset left Fig. 4). Specific sensitivity to oxygenated functions attached at the surface of the nanotubes were reported; the peak at approximately 288.5 eV corresponds to (C=O) π^* resonance in CNT–(OH–C*=O) or CNT*–(OH–C=O) (C* corresponds to the photoexcited carbon atom) [27]. In our samples, we assign this peak to the carbon 1s $\rightarrow \pi^*$ transitions of the carbonyl groups in agreement with the infrared results. These transitions are still present after vacuum annealing but with a very small intensity showing the decreasing of the oxygenated surface defects after purification in agreement with infrared results. NEXAFS spectroscopy appears to be more sensitive to oxygenated defects than infrared where carbonyls are not clearly detected after purification, but is not sensitive to the presence of hybridized carbon sp^2 impurities. Furthermore the C K edge of sample PS1 displays a huge additional contribution at 290.4 eV (Fig. 4 right inset). This peak could be assigned either to σ^*(C–O), σ^*(C–OH) contribution [27] or to a σ^* unfilled C dangling bond in vicinal position of a group O^-–C=O. This peak is not appearing in the literature when a wet oxidation of the CNTs is carried out [27–29]. It seems to mean that even if the air used for the oxidation treatment is dried, traces of water during air removal induce the formation of C–O, C–OH or O–C=O. These NEXAFS carbon resonances from 290 to 291 eV agrees with the observed σ^*(C–O) resonance of model compounds as 9-phenanthrol and xanthene [29]. This result suggests that the dry oxidation induces the formation of C–O, C–OH or O–C=O at the surface of the carbon nanostructures. Fig. 5 shows the O K-edge spectra for pristine PS0, SWCNT after HCl treatment PS2 and vacuum annealing PS3 samples, respectively. The spectra confirm the presence of oxygen-containing functional groups at each step.

The strong and sharp π^* excitation around 532 eV corresponds to carbonyl groups C=O [28–29]. The broad excitations between 538 and 550 eV are assigned to 1s σ^* resonances [27]. The decreasing intensity of the spectra following the different treatments confirms the decreasing of the number of oxygenated surface defects after each of the different steps of purification. These tendencies are well correlated with the evolution of the ν(C=O) after vacuum annealing. After oxidation and HCl treatment, the weak π^* excitation around 535 eV signs the presence of hydroxyl groups. After vacuum annealing, this hydroxyl fingerprint disappears, whereas a small amount of π^* C=O excitation remains. Hydroxyl oxygenated defects seem to be sensitive to the vacuum annealing supposed to rebuild the hexagonal carbon sp^2 surface.

3.1.4. *XPS*

The Fig. 6 shows the XPS wide scan of the CNTs powder as purchased, and after each treatment, respectively. On the virgin sample PS0, besides carbon (C 1s) as main core level contribution, the spectrum displays weak O1s, Y3d and Ni 2p contributions. More accurately, a main and wide O1s signal peaks at 532.75 eV that might correspond to either carboxylate or to hydroxyl groups, whereas a weak tail around 531 eV is due to yttrium oxide contribution (Supplementary Information SI1) with Y3d features at 156.4 and 158.25 eV (with 1.75 eV spin–orbit coupling), respectively, attributable to oxide and carbide contributions [30]. The Ni 2p3/2 contribution at 852.7 eV might correspond to either a metallic or a carbidic form. After the oxidation treatment (sample PS1), both O, Ni and Y contributions are markedly increased (Fig. 6), as monitored by the O/C, Ni/C and Y/C atomic ratios reported in Table 1. There are now three distinct contributions for oxygen O1s: one at 529.5 eV (intense and narrow) corresponding to oxidation of nickel into NiO; another at 531.7 eV (intense and wide) corresponding to functionalized oxygen-containing groups like carboxylate, quinone, lactone ... [31] and a last one at 533.8 eV (weak) that might be attributed to adsorbed oxygen or hydroxyl groups (alcohols, phenol, hydroquinone, ...) on the nanotubes. However it should be reminded that dried air is used here and that carboxylation on a graphite surface is easier than the water chemisorption. Thus it is believed that the calcination treatment leads mainly to carboxylation. This is supported by the C1s spectra reported in Fig. 7. The C1s contribution generally exhibits one single and narrow (FWHM < 1 eV) contribution at 284.6 eV (Figs. 7A–C, and Table 1). This binding energy is clearly ascertained to graphitic species (either as graphite or fullerenes, SWCNTs, amorphous carbon, adventitious carbon, graphitic and carbon nanoparticles, ...) [30]. It is not possible to separate between these later different contributions, owing to the experimental resolution of our spectrometer. Other quite noticeable contributions are however present after the oxidation treatment at higher binding energies, one at 285.2–285.4 eV and another one at 289.2 eV (sample PS1 on Fig. 7A). They represent 35% and 10% of the total carbon signal, respectively. It could be supposed that the break of a sp^2 C–C bond through carboxylation will create dangling bonds for the carbons in the vicinity of this carboxylate. These dangling bonds may also be filled with oxygen to form a phenol or a conjugated quinonic C=O bond displayed in Fig. 8. Anyway the local electronic structure of carbon atoms inside a graphitic network, either unfilled or bonded with oxygen, is deeply disturbed. If a carbon atom is bonded to an oxygen a charge transfer from carbon to oxygen directly occurs, resulting in an increase of the binding energy. If the carbon atoms are unfilled, the removal of the delocalization effect by π electrons in the screening of the C1s core hole created by the photoemission process also implies an increase of the binding energy. Finally a rehybridization of the carbon orbitals around a carbon vacancy, forming sp^3-like carbon coordination, can also explain this upward shift of 1 eV [32]. The high energy C1s contribution at 289.2 eV could be attributed to carboxylate $-COO^-$ or –COOH species [30]. In conclusion the contribution around 285.3 eV could be attributed to an unfilled carbon, a sp^3-like carbon or more probably to an oxygen-stabilized conjugated carbon in the vicinity of this carboxylate group like quinone or hydroxyl bonds.

The atomic ratio O1s/C1s, initially at 5%, rises to around 33% after the oxidation treatment (Table 1). This strongly supports notable carboxylation after the oxidation treatment. The ratio of the two carbon contributions at high energy is then 3.5, not far from the ratio of 3 for the carbon atoms in the vicinity of the carboxylate function as illustrated in

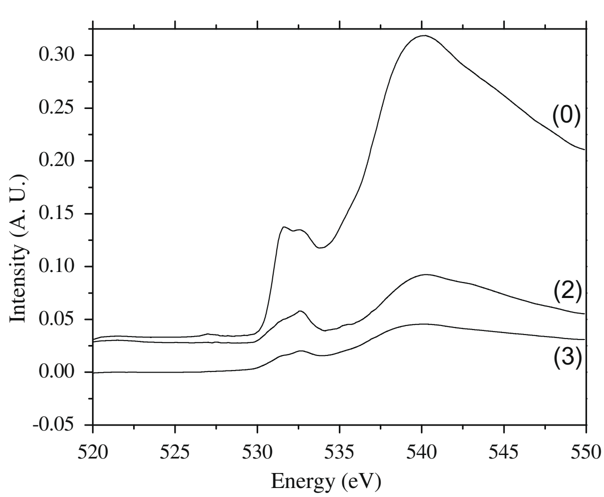

Fig. 5 – O K-edge NEXAFS spectra of the SWCNTs at the different step of the purification process. (0) PS0; (2) PS2 and (3) PS3b samples, respectively.

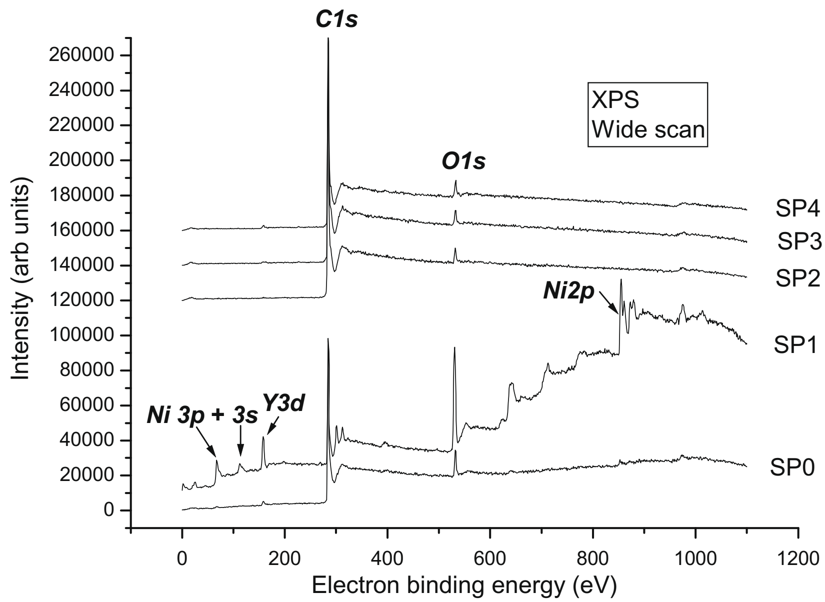

Fig. 6 – Sequence of XPS wide scan of the PS0, PS1, PS2, PS3a and PS3b samples, respectively.

Table 1 – Relative surface atomic concentrations deduced from XPS analyses.

Sample	C1s FWHM at 284.6 eV (eV)	O/C (at/at) (%)	Ni/C (at/at) (%)	Y/C (at/at) (%)
PS0	0.95	5	0.2	0.4
PS1	–[a]	31	4.7	5.4
PS2	0.75	3	<0.1	0.1
PS3a	0.8[b]	3	<0.1	0.1
PS3b	0.9[b]	4	<0.1	0.2

a Three contributions as seen in Fig. 7A.
b Four contributions as seen in Fig. 7C.

Fig. 8 in the case of the formation of a simple carboxylate function. After the acid and the annealing treatments, the O1s/C1s ratio drops abruptly to some percents, indicating large oxygen removal (Table 1). Accordingly, the two high energy carbon contributions are mainly removed (Fig. 7C). The remaining small contribution shifted to 290.2 eV is believed to be now more representative of an electron loss contribution due to ($\sigma + \pi$) plasmon excitation of a graphitic structure.

Concerning metals, the main nickel 2p core level displays a positive energy shift by 1.05 eV after oxidation corresponding to the formation of NiO (see Supplementary Information SI2) whereas the yttrium contribution does not display any shape modification. After the subsequent acid treatment (sample PS2), the oxygen, nickel and yttrium signals drop abruptly. The O1s signal is now centered around 532.4 eV with a large full width at half maximum (FWHM) of 3.2 eV (see Supplementary Information SI1). Thus it is believed that two close contributions may exist, which have been tentatively localized around 532.15 eV and around 533.4 eV by shape analysis. While the former one could be assigned to oxygen bonded to carbon, the latter can be better explained by physisorbed oxygen. A residual contribution at low energy (<530 eV) may be attributed to traces of Y_2O_3. Following the treatments at 1100 and 1400 °C (sample PS3a and PS3b, respectively) no special evolution can be observed.

However a high energy C1s contribution is again present after the high thermal treatment at 1400 °C, which represents no more than 20% of the total signal. The weak O1s signal shifts to higher energy at 533 eV is due to a more important contribution of physisorbed oxygen. The exact origin of this carbon contribution around 285.3 eV is not completely known. It is presumably not the same as the thermal treatment is rather known to suppress the defects on a graphite-type surface. It is possible either that carbonaceous residues are cracked at high temperatures into the furnace, or that species like oxycarbide [33] (case of yttrium) can then be obtained.

3.1.5. *Discussion on spectroscopic results*

The above results give a qualitative and quantitative analysis of the level of surface oxygenated groups that have been introduced or removed throughout the purification procedure as well as the level of metallic impurities. We have seen that the pristine sample contains a non negligible number of oxygenated groups. After the first oxidative step, two important observations can be noticed: (i) a quantitative increase of the level of oxygenated groups involving mainly carboxylate, phenol and quinone groups and (ii) the oxidation of the metallic catalysts. Regarding the Raman spectra, we do not observe an increase of the D-band intensity (with respect to the G band) meaning that the vibrational modifications due to the oxidation treatment is weak. The preserved conjugated character of the product of oxidation like the one displayed in Fig. 8 may explained this weak disturbance of the Raman spectra. NEXAFS and XPS results are in good agreement to predict the formation of carboxylate to hydroxyl or carbonyl groups with a ratio of around 25–30%, considering the overall

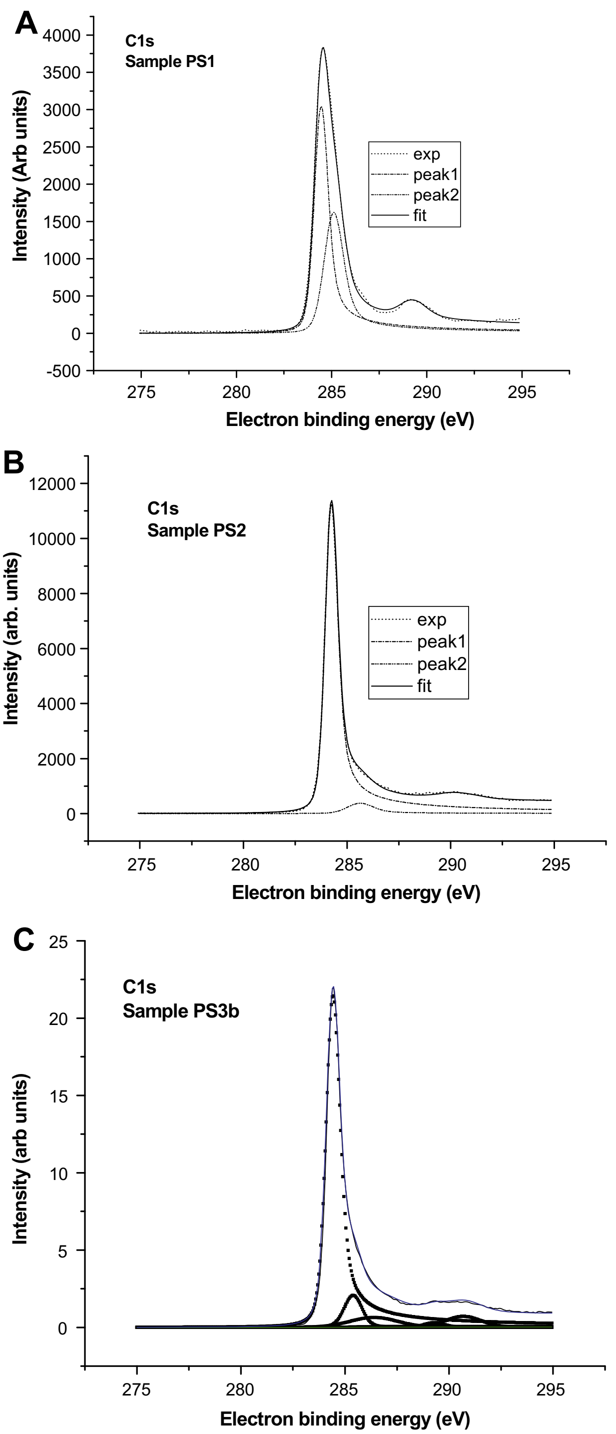

Fig. 7 – XPS spectra of the C1s level of the samples. (A) PS1; (B) PS2 and (C) PS3b samples, respectively. Spectra are fitted with Voigt functions. The contribution of background is not displayed.

carbon content. This is in agreement with the total of oxygenated functions which represents around 30% from the O/C (at/at) XPS ratio. After step ii and in agreement with the reductive character of the HCl treatment, the number of oxygenated functions is drastically reduced. This is evidenced using NEXAFS, IR and XPS investigations. The acid treatment does not induce significant damaging of the SWCNTs because the intensity of the D-band (see Raman and IR spectroscopy results) is not highly modified after step ii. HCl is known to be less destructive towards the SWCNTs than HNO_3, for example [15]. Surprisingly, the results suggest that high temperature annealings induce again a weak damaging of the SWCNTs, instead of an expected improvement of their surface quality. However, interpretation of the results is still complicated due to the difficulty to separate the signal coming from the different carbonaceous species in the sample. Further investigations using other complementary techniques more sensitive to the structure of each component in the samples such as XRD, TGA and TEM allow going in more details regarding the effect of the chemical treatments towards the SWCNTs.

3.2. *Modification of structure and composition of the samples through the chemical treatments*

3.2.1. *X-ray diffraction*

3.2.1.1. Sample transformations viewed by diffraction. The diffraction pattern of the raw SWCNT sample PS0 is shown in Fig. 9. This diagram is dominated by strong reflections from nickel nanoparticles of mean size ~11.0 nm as deduced from their widths. A strong "background" at small wave-vectors Q below 1 $Å^{-1}$ is visible. In fact this is not a "background" but an intrinsic signal which indicates that the sample contains nanoparticles. The (10) reflection of the SWCNT bundles appears as a bump in this nanoparticles "background". A weak peak at about 1.8 $Å^{-1}$ indicates that the powder contains some graphitic particles.

The diffraction pattern of the powder after the oxidation step (PS1) displays very intense peaks of new nano-crystallized particles which are identified as NiO from their positions (cfc, $a = 4.18$ Å). The mean particle size is the same as that of the Ni particles in PS0 sample. This demonstrates that Ni particles transform into NiO during oxidation. However, weak reflections from metallic nickel are still visible but with a narrower shape. One deduces a mean Ni particle size larger than 40 nm for the remaining Ni contained in the powder. If the peak of graphitic particles is still distinguishable, the (10) reflection from bundles is completely diluted into the small Q signal of the NiO nanoparticles.

After the acid treatment most of NiO particles are removed (PS2 diagram in Fig. 9), but the large Ni particles are again visible. The (10) reflection and other (hk) reflections of the SWCNT bundles are now clearly distinguishable. The strongest peak at 1.8 $Å^{-1}$ in the diagram is attributed to graphitic particles. It presents two components. The right-hand side one is due to graphite-like particles: the number of graphene sheets, plane or curved, is large enough to ensure a small width to the peak. The left-hand side component is wider. It is attributed to nanographite (plane or curved), more or less organized. We distinguish therefore two populations of graphitic-like compounds, one which is rather large and well-organized and the other one which is rather small and poorly organized.

After annealing the powder, the (hk) reflections from bundles become even more pronounced. However the sample contains a large amount of remaining graphitic particles. In sample PS3a (thermal treatment at 1100 °C) the nickel peaks are still visible (Fig. 10). In sample PS3b (treatment at

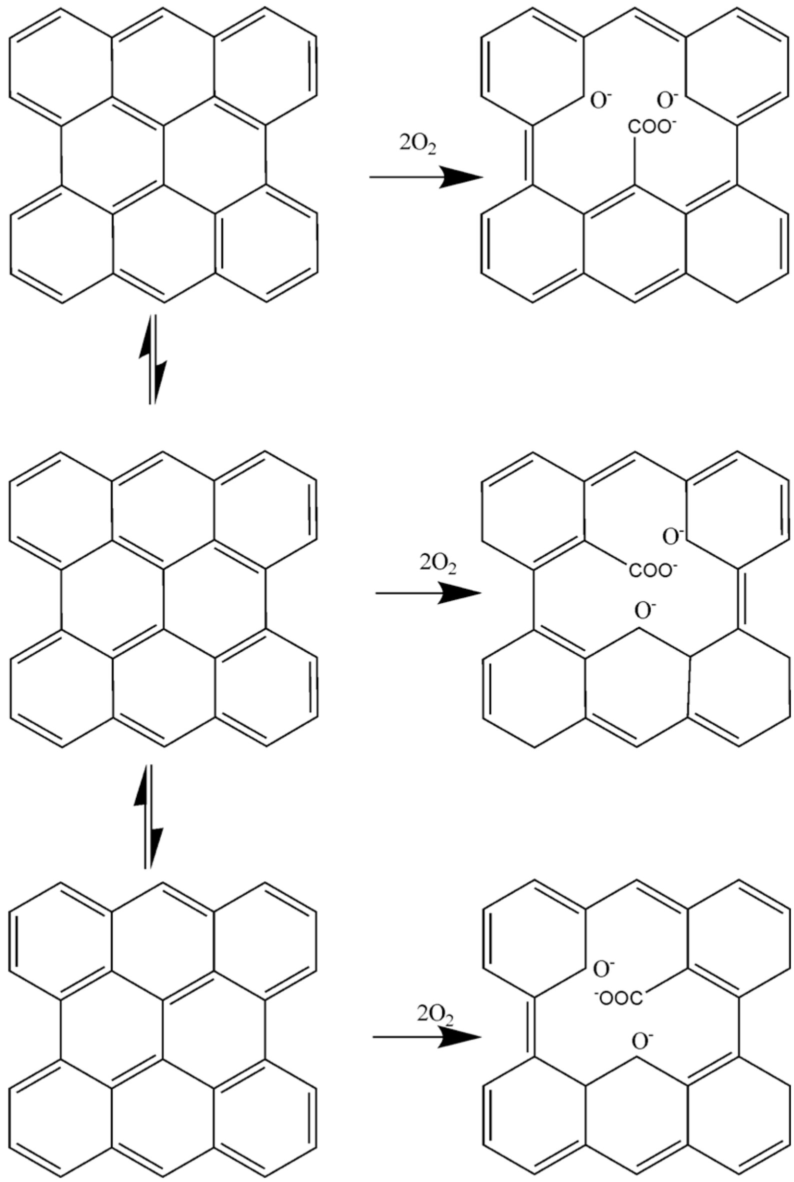

Fig. 8 – A scheme for dry oxidation of single-wall carbon nanotubes.

1400 °C – Fig. 9) the nickel peaks are no longer observed in the diffraction pattern but new weak peaks of unknown crystallized impurities appear (at 2.04 and 3.35 Å^{-1} as examples). As they are weak they represent only a small fraction of the powder mass.

A simulation of the SWCNT diffraction pattern for $Q < 2\ \text{Å}^{-1}$ has been done so as to reproduce the data in the PS3a sample (see the dotted line in the inset of Fig. 10) [34]. It gives the following characteristics: mean diameter 14.6 Å, mean tube-tube distance 17.8 Å, width of diameter distribution (supposed to be Gaussian) 2 Å and mean bundle size of ~20 tubes. To estimate the relative fraction of each species in our samples we further performed a simulation of the diffraction pattern for the different steps of the purification treatment.

3.2.1.2. Brief model description [34]. We consider 5 different compounds referred as: (i) nickel and (ii) NiO nano-crystals; (iii) large and well-organized graphite particles, (iv) small and poorly organized graphitic-like particles or ribbons (both of these last species may include ribbons and individual nanotubes) and (v) SWCNT bundles. Of course this classification will neglect amorphous carbon or badly organized carbonaceous impurities. In each case we calculate: (i) the Fourier transform of the object considered (ex. a nanocrystal) in reciprocal space and (ii) the space averaging of the intensity of the diffraction signal which is the square modulus of (i) [34]. Each contribution is conveniently scaled according to the data providing that a "background" in ($1/Q^n$) has been subtracted to the experimental curves shown in Fig. 10 to make the (hk) reflections of SWCNT bundles appearing. The graphitic-like species (iii–v) have been considered to be made with continuous surfaces of graphene sheets where the carbon atoms have been replaced by a uniform density of scatterers [35]. An example of this model applica-

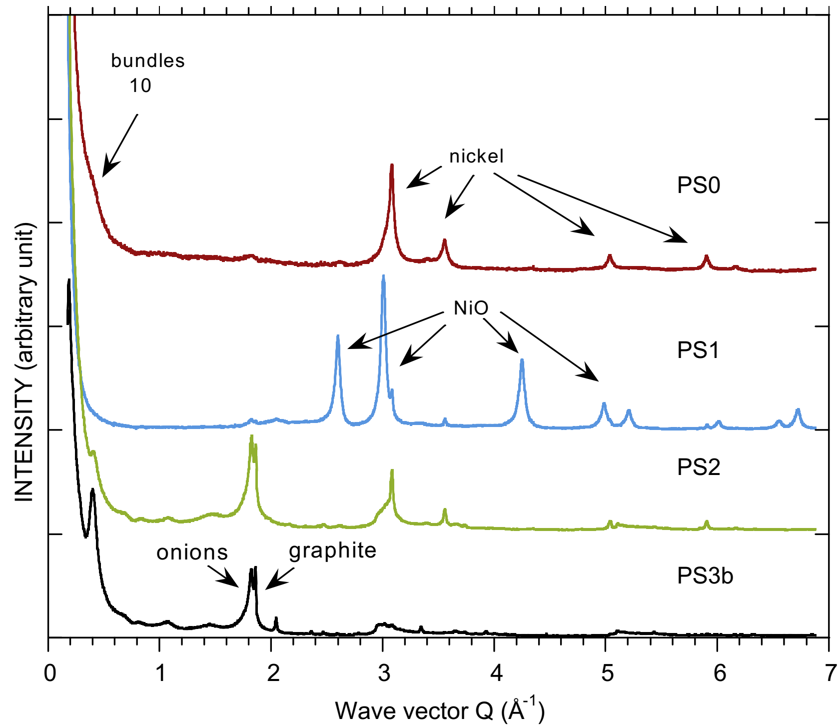

Fig. 9 – Diffraction patterns of the PS samples.

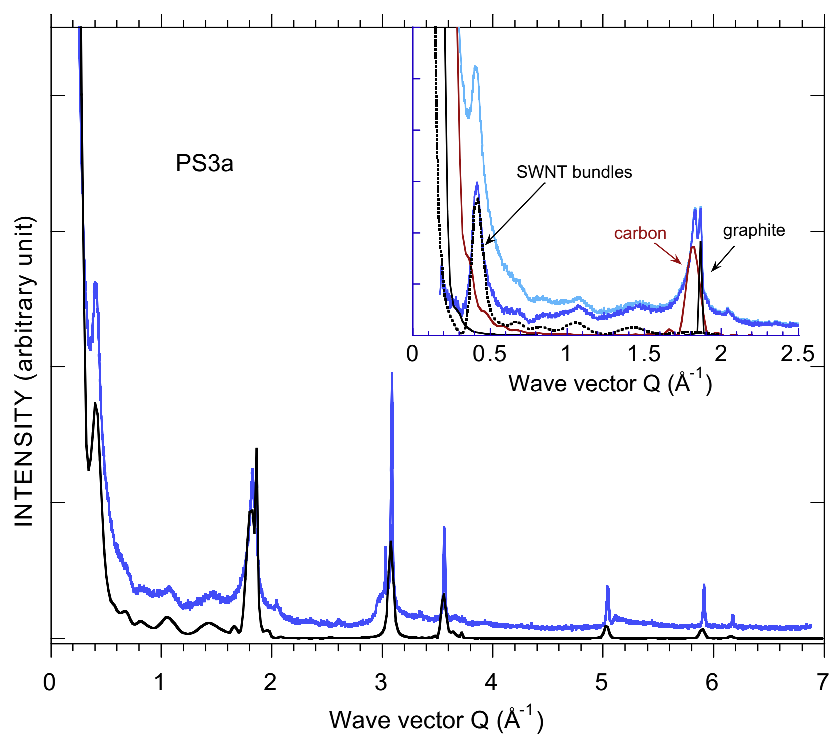

Fig. 10 – Application of the simulation to the PS3a sample. The simulated curve is below the experimental one. Inset: details of the diagram with two experimental curves (above, see the text for the meaning of each of these curves) and simulation (below) for SWCNT (dotted line), graphite species and graphitic-like (carbon) species.

tion is shown in Fig. 10 for the PS3a sample. The black curve below the experimental one is the sum of the five contributions. The agreement with the data is reasonable. The inset shows the different contributions from: graphite large particles (iii), small graphitic particles (iv) and SWCNT bundles (v). Two experimental curves are shown. One is the direct measured pattern and the other is the same after "background" subtraction.

As we know the number of atoms of each species introduced into the simulation of the diffraction pattern we are able to calculate the sample composition for the different samples. However the results obtained from such simulation strongly depend on the hypothesis, i.e. the object used to represent each species. Particularly we do not know the exact structure of the small graphitic-like species (either particle or ribbon or single nanotube). Some molecules or elements like Y, carboxyl groups, oxygen, have not been considered in the simulation. Consequently the errors on the sample composition obtained by this method are large. We estimate the errors to ±33% (example: Ni content is 45 ± 15% for PS1).

3.2.1.3. Composition of the sample at the different steps. Fig. 11 gives the composition in atomic percentage for the different samples. In sample PS1 the nickel content comprises the Ni atoms both of Ni particles and of NiO nano-crystals. In each histogram carbon refers to species (iii). In the raw sample PS0 the SWCNT bundles represent ~1/3 of the total atomic composition. The nickel content is a very large: ~20%. The rest is graphite or graphitic-like species. After the oxidation treatment the SWCNT content strongly decreases down to 10–15 at.%, whereas the graphite and graphitic-like species remain approximately at the same level. Accordingly it appears that the most fragile carbon compound during the oxidation treatment is SWCNT species. Such behaviour has been previously reported [36]. The PS1 sample is made up of ~ 50 at.% of Ni and NiO particles in good agreement with the TEM results.

The acid treatment (PS2 powder) removes almost completely the nickel. However the SWCNT content seems to decrease again (5 at.%). This apparent new decreasing of the tubes content could be explained by an experimental artifact. In fact we use the same curve for the simulation of the SWCNT contribution in the four samples, the curve shown

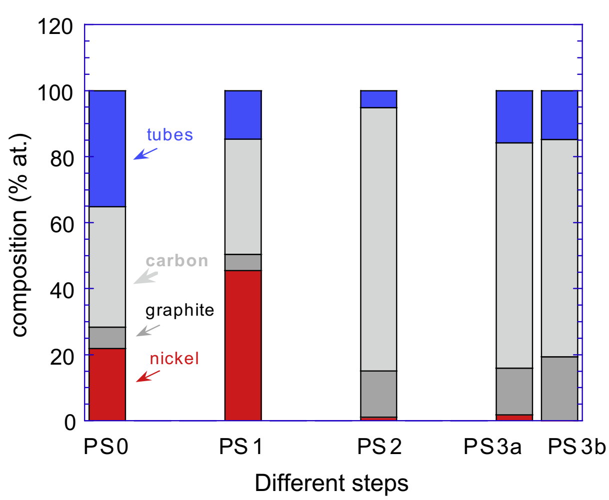

Fig. 11 – Histogram of the composition of the samples deduced from XRD line analysis (at.%).

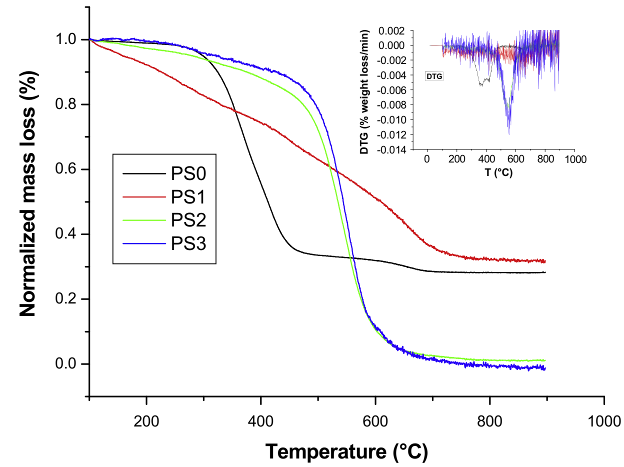

Fig. 12 – Normalized mass loss monitored by TGA on samples PS0, PS1, PS2 and PS3b, respectively. In inset the DTG curves are displayed for samples PS0, PS2 and PS3b.

in the inset of Fig. 10. It could happen that during the preparation of the PS2 sample the SWCNTs are filled with some liquid phase in their inner volume. It is well known that in this case the intensity of the (10) reflection strongly decreases [37], thus decreasing the apparent content of tubes in the sample. Finally after annealing the powder under vacuum, the final sample is made of ~15 at.% of SWCNTs and ~85 at.% of graphite and carbon. Despite the fact that the simulation gives only an estimation of the sample composition we emphasize two results: (i) SWCNTs are more fragile than other graphitic particles during oxidation and (ii) the final powder contains more graphitic species than true SWCNT bundles.

3.2.2. *TGA*

The Fig. 12 displays the TGA curves of samples PS0, PS1, PS2 and PS3b, corresponding to the different steps of purification. The mass rates are normalized in order to provide a direct comparison. In the inset of Fig. 12 the differential thermograms (DTG) of PS0, PS2 and PS3b are shown. The salient features extracted from these curves are presented in Table 2, i.e. the maximum combustion rate extracted from the DTG curves as well as the remaining mass at 900 °C which is believed to be characteristic of the catalyst (Ni and Y) initial content. The main loss of mass corresponding to carbon combustion is strongly shifted at higher temperatures after the oxidation treatment. The as-received sample PS0 exhibits a

Table 2 – TGA analyses.

Samples	Maximum of weight consumption from DTG (°C)	Relative remaining weight at 900 °C (weight%)
PS0	372, 417	28
PS1	–	33
PS2	539	1.2
PS3b	555, 645	0.8

main combustion temperature in the range 350–420 °C, corresponding to the Ni-catalyzed combustion of highly disordered graphitic carbon, amorphous carbon or SWCNTs [38–40]. Another small mass consumption occurs around 630 °C. It could correspond to weak non-catalyzed carbon combustion. After the oxidative step the TGA curve is quite modified with continuous mass consumption starting soon from 100 °C up to 700 °C. This supports the formation of carbon sites highly reactive for oxidation through either functionalization or formation of carbon vacancies in the graphite cyclic network. The presence of the catalyst is supported by the remaining mass at 900 °C around 30%. After the acid treatment, the main combustion temperature is shifted to around 540 °C. This large shift can be due to the dissolution of the catalyst. This is supported by the remaining mass which is now only around 1%. After the high temperature treatment, the main consumption temperature is slightly shifted to 555 °C, corresponding to the combustion of more ordered graphitic carbon like SWCNT or graphite particles, whereas the small contribution at 645 °C can be attributed to the combustion of larger graphitic nanoparticles or onions.

3.2.3. *TEM analysis*

We only show here one typical TEM image for each sample (Fig. 13). As for typical as-synthesized arc-discharge samples, SWCNTs are assembled in bundles of several tens of tubes and a non negligible quantity of impurities is present in the sample, including catalyst particles (nickel and yttrium) coated with amorphous carbon and more or less graphitized carbon particles (Fig. 13a). No modification of the SWCNT bundle size is noticed throughout the purification procedure. After the oxidation step (Fig. 13b), the aspect of the impurities has strongly changed. They become more homogeneous. Electronic contrast between the carbon part and the metallic part has indeed decreased meaning that both the nature and the structure of the impurities have been modified. On the contrary, the aspect of the SWCNT bundles is still similar to that of the raw sample. For the sample PS2 (Fig. 13c), after the acid treatment, the number of catalyst particles has been highly reduced. SWCNT bundles are still present. It appears numerous empty carbon shells certainly coming from the removal of catalyst particles previously confined inside them. HT treatment has not induced strong modification of the morphology of the impurities (Fig. 13d). From TEM observations, appearance of the bundles regarding the quality of the walls has only slightly changed throughout the procedure meaning that a low number of defects has been created on the tube surface, particularly after the oxidizing and acid treatments.

3.2.4. *Discussion on structural results*

TEM observations as well as XRD and TGA measurements bring additional important information at each step of the purification procedure. Similar purification procedure has been carried out by Harutyunyan et al. [38] on the same sam-

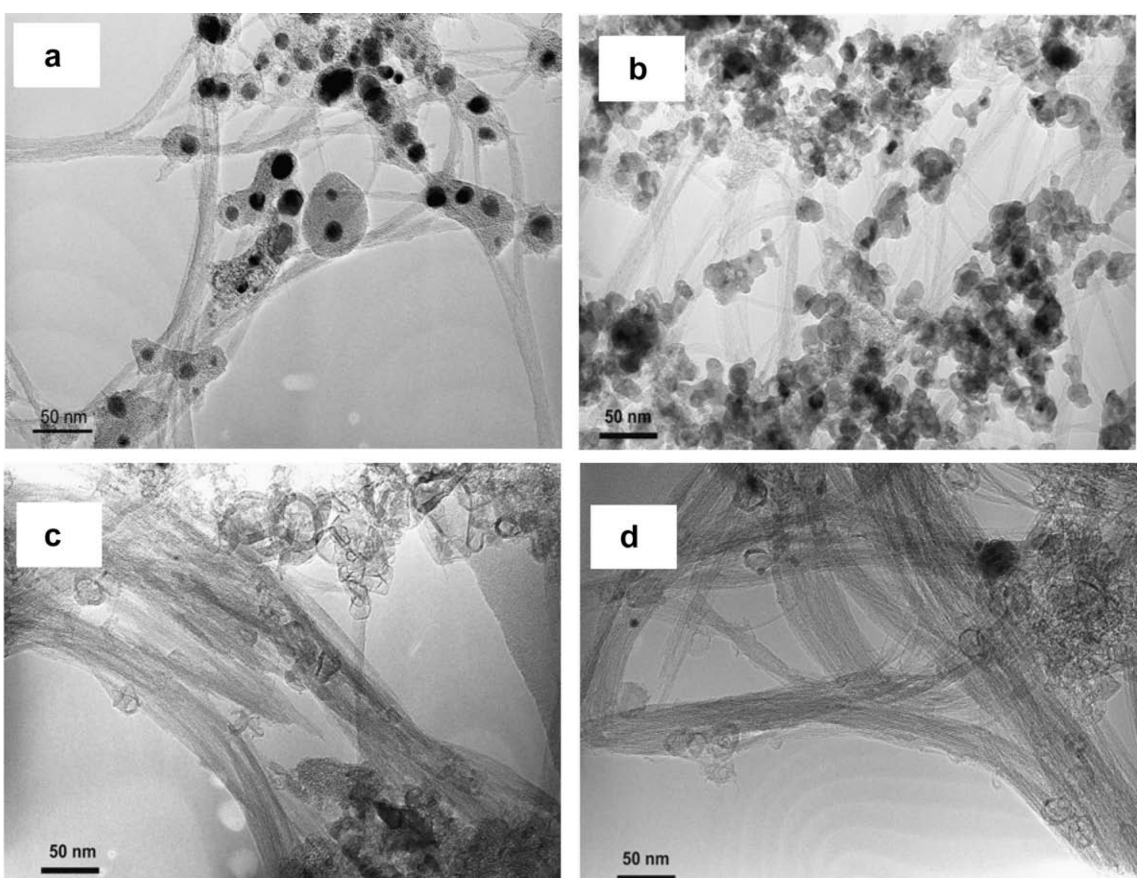

Fig. 13 – TEM images of the samples after each step of the purification procedure. (a) Raw sample PS0; (b) after dry air oxidation PS1; (c) after acid treatment PS2; (d) after HT annealing PS3a.

ple. Therefore some results can be directly compared. On the pristine sample they found about 29% (weight) of nickel and yttrium remaining as catalytic impurities, which means around 8 at.%, considering Ni mainly in a metallic state as evidenced by XPS. This is in fairly good agreement with the result found by TGA. By XRD we get from the intensity line analysis around 20 Ni at.%. This overestimation of the nickel concentration is not completely understood but it could be explained by a number of unexpected effects such as orientational effects of carbonaceous species or by the selectivity of the XRD intensity lines to the size effect. After the oxidation step on sample PS1, the remaining metallic impurities rise to 33% instead of 28%. This increase of the metallic impurities at this step can be explained in two ways: the transformation of Ni into NiO and some combustion of carbon occurring during the step of oxidation, leading to some relative enrichment of the concentration of metallic impurities. It should be noted the good agreement between XRD, TEM and XPS concerning the change of the nature of the Ni impurity as they all predict a noticeable Ni oxidation. After the acid treatment, the results show that the large majority of nickel and yttrium is etched away. The removal of the catalysts has consequence on the thermal stability of the samples, as indicated by the shift of the combustion towards higher temperatures.

Concerning the different carbon phases present at each step of the purification process, we have compared the results of ref 38 with our TGA and XRD data. According to [38], the amorphous carbon, the nanotubes and the graphitic nanoparticles are successively consumed at 350, 395 and 420 °C in proportions which are roughly quoted to 45%, 45% and 10%, values which are to be compared with the results of TGA and DTG (Fig. 14a, PS0 sample). TGA curve exhibits three consumption peaks at 372, 417 and 630 °C with proportions roughly 47%, 47% and 6%, respectively, and the XRD line intensity analysis previously described gives concentrations of 45%, 47% and 8%, respectively. The small shift (ca 20 °C) obtained between the two TGA experiments can be explained by different temperature raising rate and initial masses. It is therefore tempting to assignate the two first peaks to the burn off of carbon nanotubes bundles and of weakly organized

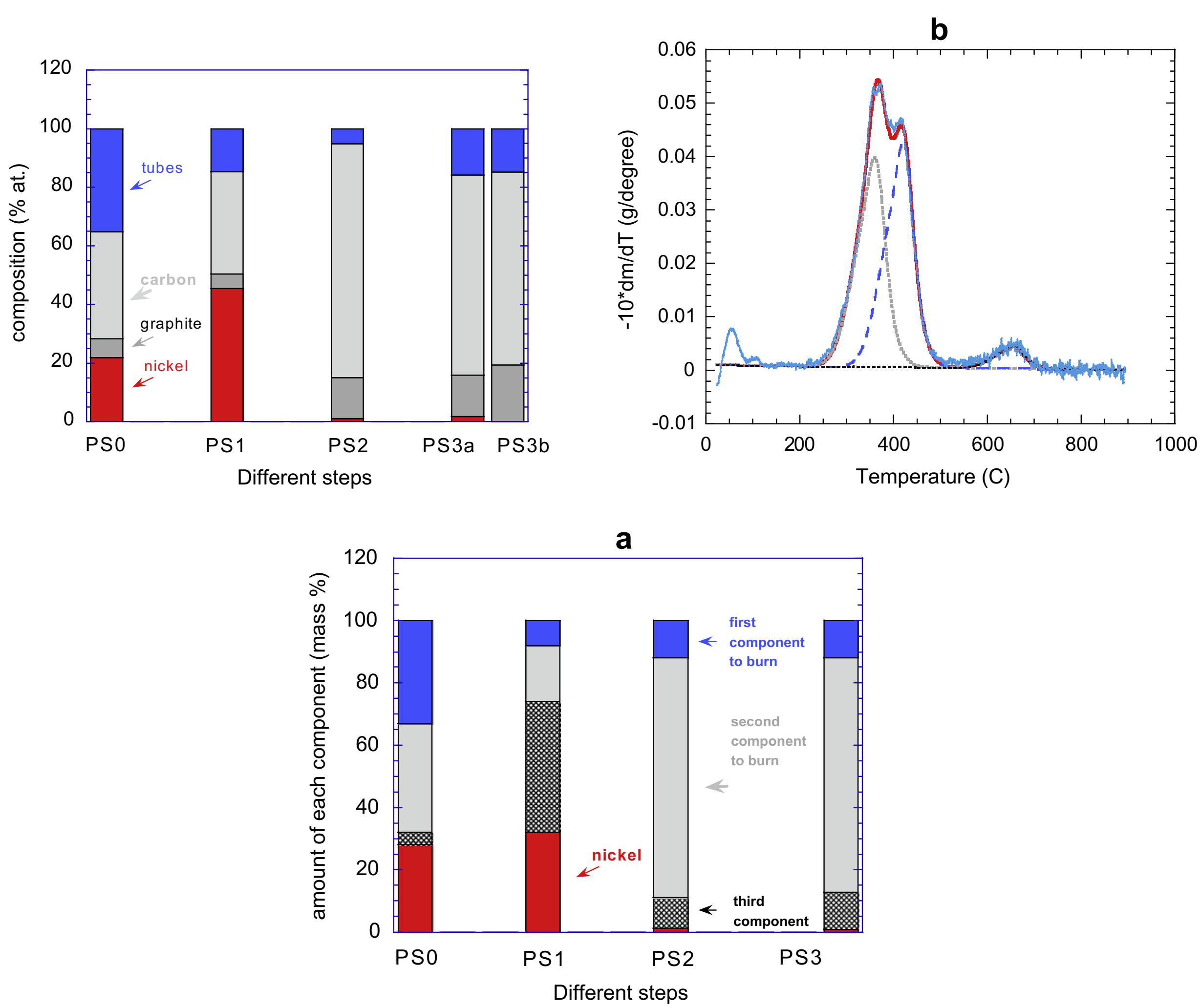

Fig. 14 – (a) Relative proportions of the different components deduced from TGA and DTG in the four samples. The results are to be compared with the histogram of Fig. 10 (displayed here only for sake of discussion); (b) inversed DTG curve of the PS0 sample. The continuous curve superposed on data points is the sum of the three components indicated by dash and dotted curves.

graphitic-like species in the presence of nickel catalysts. In a recent paper Miyata et al. [36] have found that SWCNTs were the first species to burn during a TGA experiment, in contradiction with previous and current interpretations on as-grown samples, not yet treated with acid treatment. As the relative abundance of the two first species to burn, namely amorphous carbon and SWCNTs, are comparable in our PS0 sample it is not possible to attribute the two peaks in the DTG curve (see Fig. 13b) on the base of the XRD results. So we decided to analyse all TGA and DTG results with the three peaks model for carbon species depicted on Fig. 14b. The results are presented in Fig. 14a where the relative proportions of the different components (in mass%) are shown for the four samples. A comparison with the similar diagram obtained from XRD (Fig. 9) is very instructive as apart the overestimation of Ni content in the XRD results of PS0 and PS1 samples which has been previously explained, it clearly displays some common behaviours. It appears that the first component to burn corresponds to the SWCNTs (see PS2 and PS3 samples in Figs. 8 and 13a, respectively). Consequently the second, very large component is attributed to amorphous carbon or weakly organized graphitic-like species and the third one to graphitic particles, in agreement with Miyata et al. [36].

4. Conclusions

Arc-discharged produced SWCNTs have been submitted to a commonly used three-step purification procedure. Purification of CNT samples is still a tricky task particularly because of the variety of impurities in the samples including more or less graphitized carbon particles and metallic catalysts. In this work, the samples were characterized throughout the chemical treatments by the means of techniques sensitive to both the nature and the quality of the SWCNT surface and to the concentration of the different species in the samples. The obtained results shed in light the critical steps for the efficiency of these procedures. The first oxidation treatment is of crucial importance for the success of the procedure because it is supposed to selectively remove the amorphous carbon particles and poorly attack the SWCNTs for the used experimental conditions. Nevertheless, it appears that SWCNTs are as sensitive to oxidation as the carbonaceous impurities. This result gives the limitation of such purification procedure. This first step however also allows an efficient oxidation of the catalyst particles that can further be easily solubilised in the acid solution at the second step of the procedure. To remove the surface groups introduced during these two previous steps which are mainly carboxyl, hydroxyl and carbonyl groups, the optimization of the final annealing treatment remains subtle. Other preliminary steps allowing for a direct catalyst oxidation at low temperatures must indeed be explored, such as O_2 plasma treatment or strong liquid or gas oxidations in order to improve the relative rate of consumption of carbon impurities.

Acknowledgements

D. Burger (IPCMS/GMI) is acknowledged for TGA analyses. The authors would like to thank J. Lambert his technical help for XPS experiments and B. Doyle for NEXAFS measurements at Elettra, Trieste.

Appendix A. Supplementary data

Supplementary data associated with this article can be found, in the online version, at doi:10.1016/j.carbon.2009.10.044.

REFERENCES

[1] Loiseau A, Gadelle P, Peigney P, Blase X, Charlier JC, Ducastelle M. Growth mechanism of carbon nanotubes. In: Loiseau et al., editors. Understanding carbon nanotubes: from theory to applications. Berlin: Springer; 2006. p. 49–78.
[2] Hou PX, Liu C, Cheng HM. Multi-step purification of carbon nanotubes. Carbon 2008;46:2003–25.
[3] Chen J, Hamon MA, Hu H, Chen Y, Rao AM, Eklund PC, et al. Solution properties of single-walled carbon nanotubes. Science 1998;282:95–8.
[4] Li F, Cheng HM, Xing YT, Tan PH, Su G. Purification of single-walled carbon nanotubes synthesized by the catalytic decomposition of hydrocarbons. Carbon 2000;38:2041–5.
[5] Yu Z, Brus LE. Reversible oxidation effect in Raman scattering from metallic single-wall carbon nanotubes. J Phys Chem A 2000;104:10995–9.
[6] Zhang M, Yudasaka M, Koshio A, Iijima S. Effect of polymer and solvent on purification and cutting of single-wall carbon nanotubes. Chem Phys Lett 2001;349:25–30.
[7] Moon JM, An KH, Lee YH, Park YS, Bae DJ, Park GS. High-yield purification process of single walled carbon nanotubes. J Phys Chem B 2001;105:5677–81.
[8] Grimes CA, Dicky EC, Mungle C, Ong KG, Qian D. Effect of purification of the electrical conductivity and complex permittivity of multiwall carbon nanotubes. J Appl Phys 2001;90:4134–7.
[9] Chattopadhyay D, Galeska I, Papadimitrakopoulos F. Complete elimination of metal catalysts from single wall carbon nanotubes. Carbon 2002;40:985–8.
[10] Yang CM, Kaneko K, Yudasaka M, Iijima S. Effect of purification on pore structure of HiPco single-walled carbon nanotube aggregates. Nano Lett 2002;2:385–8.
[11] Banerjee S, Wong SS. Rational sidewall functionalization and purification of single-walled carbon nanotubes by solution-phase ozonolysis. J Phys Chem B 2002;106:12144–51.
[12] Zhao W, Song C, Zheng B, Liu J, Viswanathan T. Thermal recovery behavior of fluorinated single-walled carbon nanotubes. J Phys Chem B 2002;106:293–6.
[13] Strong KL, Anderson DP, Lafdi K, Kuhn JN. Purification process for single-wall carbon nanotubes. Carbon 2003;41:1477–88.
[14] Sen R, Richard SM, Itkis MF, Haddon RC. Controlled purification of single-walled carbon nanotube films by use of selective oxidation and near-IR spectroscopy. Chem Mater 2003;15:4273–9.
[15] Martinez MT, Callejas MA, Benito AM, Cochet M, Seeger T, et al. Sensitivity of single wall carbon nanotubes to oxidative processing: structural modification, intercalation and functionalization. Carbon 2003;41:2247–56.
[16] Yudasaka M, Ichihashi T, Kasuya D, Kataura H, Iijima S. Structure changes of single-wall carbon nanotubes and single-wall carbon nanohorns caused by heat treatment. Carbon 2003;41:1273–80.
[17] Gregan E, Keogh SM, Mahuire A, Hedderman TG, Neill LO, Byrne HJ. Purification and isolation of SWNTs. Carbon 2004;42:1031–5.

[18] Pehrsson PE, Zhao W, Baldwin JW, Song C, Liu J, Steven K, et al. Thermal fluorination and annealing of single-wall carbon nanotubes. J Phys Chem B 2003;107:5690–5.
[19] Tran NE, Lambrakos SG. Purification and defect elimination of single-walled carbon nanotubes by the thermal reduction technique. Nanotechnology 2005;16:639–46.
[20] Furtado CA, Kim UJ, Gutierrez HR, Pan L, Dickley EC, Eklund PC. Debundling and dissolution of single-walled carbon nanotubes in amide solvents. J Am Chem Soc 2004;126:6095–105.
[21] Scofield JH. Hartree-Slater subshell photoionization cross-sections at 1254 and 1487 eV. J Electron Spectr Rel Phen 1976;8:129–37.
[22] Sbai K, Rahmani A, Chadli H, Bantignies JL, Hermet P, Sauvajol JL. Infrared spectroscopy of single-walled carbon nanotubes. J Phys Chem B 2006;110:12388–93.
[23] Bantignies JL, Sauvajol JL, Rahmani A, Flahaut E. Infrared-active phonons in carbon nanotubes. Phys Rev B 2006;74. 195425: 1–5.
[24] Natile MM, Glisenti A. Surface reactivity of NiO: interaction with methanol. Chem Mater 2002;14:4895–903.
[25] Bantignies JL, Deabate S, Righi A, Rols S, Hermet P, Sauvajol JL, et al. New insight into the vibrational behavior of nickel hydroxide and oxyhydroxide using inelastic neutron scattering, far/mid-infrared and raman spectroscopies. J Phys Chem C 2008;112:2193–201.
[26] Kim UJ, Furtado CA, Liu XM, Chen G, Eklund PC. Raman and IR spectroscopy of chemically processed single walled carbon nanotubes. J Am Chem Soc 2005;127:15437–45.
[27] Banerjee S, Hemraj-Benny T, Balasubramanian M, Ficher DA, Misewich JA, Wong SS. Ozonized single-walled carbon nanotubes investigated using NEXAFS spectroscopy. Chem Commun 2004:772–3.
[28] Kuznetsova A, Mawhinney DB, Naumenko V, Yates JT, Liu J, Smalley RE. Enhancement of adsorption inside of single-walled nanotubes: opening the entry ports. Chem Phys Lett 2000;321:292–6.
[29] Kuznetsova A, Popova I, Yates JT, Bronikowski MJ, Huffman CB, Liu J, et al. Oxygen-containing functional groups on single-wall carbon nanotubes: NEXAFS and vibrational spectroscopic studies. J Am Chem Soc 2001;123:10699–704.
[30] Mulder J. Handbook of X-ray photoelectron spectroscopy. Amsterdam: Perkin Elmer; 1982. 98.
[31] Ohta T, Yamada M, Kuroda H. X-ray photoelectron spectroscopy of *p*-benzoquinone, hydroquinone and their halogen-substituted derivatives. Bull Chem Society Japan 1974;47:1158.
[32] Constant L, Speisser C, Le Normand F. HFCVD diamond growth on Cu(1 1 1). Evidence for carbon phase transformations by in situ AES and XPS. Surf Sci 1997;387:28–43.
[33] Holcombe CE, Carpenter DA. Identification of a new yttrium oxycarbide Y_2 OC. J Am Ceram Soc 1981;64:C82–3.
[34] Rols S, Almairac R, Henrard L, Anglaret E, Sauvajol JL. Diffraction by finite-size crystalline bundles of single wall nanotubes. Eur Phys J B 1999;10:263–70.
[35] Cambedouzou J, Pichot V, Rols S, Launois P, Petit P, Klement R, et al. On the diffraction pattern of C_{60} peapods. Eur Phys J B 2004;42:31–45.
[36] Miyata Y, Yanagi K, Maniwa Y, Tanaka T, Kataura H. Diameter analysis of rebundled single-wall carbon nanotubes using X-ray diffraction: verification of chirality assignment based on optical spectra. J Phys Chem C 2008;112:15997–6001.
[37] Fujiwara A, Ishii K, Suematsu H, Kataura H, Maniwa Y, Suzuki S, et al. Gas adsorption in the inside and outside of single-walled carbon nanotubes. Chem Phys Lett 2001;336:205–11.
[38] Harutyunyan AR, Pradhan BK, Chen G, Chang J, Eklund PC. Purification of single-wall carbon nanotubes by selective microwave heating of catalyst particles. J Phys Chem B 2002;106:8671–5.
[39] Illekova E, Csomorova K. Kinetics of oxidation in various forms of carbon. J. Therm Analy Calorim 2005;80:103–8.
[40] Brukh R, Mitra S. Kinetics of carbon nanotube oxidation. J Mater Chem 2007;17:619–23.